Unexpected thermal aging effect on brittle fracture and elemental segregation in modern dissimilar metal weld

Materials Characterization 217 (2024) 114419

Contents lists available at ScienceDirect

Materials Characterization

journal homepage: www.elsevier.com/locate/matchar

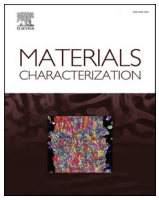

Unexpected thermal aging effect on brittle fracture and elemental segregation in modern dissimilar metal weld

Andrea Fazi [a], Pedro A. Ferreirós [b], Yanling Ge [b], Song Lu [c], Mattias Thuvander [a], Zaiqing Que [b,*]

[a] Microstructure Physics, Department of Physics, Chalmers University of Technology, 412 96 Göteborg, Sweden
[b] Advanced Materials for Nuclear Energy, VTT Technical Research Centre of Finland, Kivimiehentie 3, 02150 Espoo, Finland
[c] Integrated Computational Materials Engineering, VTT Technical Research Centre of Finland, Vuorimiehentie 2, 02044 Espoo, Finland

ARTICLE INFO

Keywords:
Dissimilar metal weld
Thermal aging
Segregation
Carbide
Fracture

ABSTRACT

A full-scale dissimilar metal weld safe-end mock-up, precisely replicating a critical component of a modern nuclear power plant, was investigated. The brittle fracture behavior, carbide evolution and nanoscale elemental segregation in the heat-affected zone (HAZ) of low alloy steel (LAS) were analyzed under both post-weld heat-treated and thermally-aged conditions (400 °C for 15,000 h, equivalent to 90 years of operation) using analytical electron microscopy and atom probe tomography. The observed increase in grain boundary (GB) decohesion and intergranular cracking on the fracture surface and the decrease of fracture toughness are primarily attributed to P and Mn segregation to GBs and the coarsening of carbides upon long-term thermal aging. The direct observations of significant elemental segregation to GBs and the consequent reduction in fracture toughness in the HAZ are unexpected for modern low-phosphorus LASs, highlighting potential concerns for evaluating the structural integrity of modern nuclear power plants.

1. Introduction

Dissimilar metal welds (DMWs) are routinely employed to join bainitic/ferritic low alloy steel (LAS) reactor pressure vessel with austenitic stainless steel pipes using Ni-based filler metals [1–3]. The differing chemical composition, crystal structure and mechanical properties at the fusion boundary (FB) create a mismatch [4–7]. DMWs can become a concern for the structural integrity in nuclear power systems, structures and components (SSC). A couple of failures have been observed in DMWs in nuclear power plants [8–10]. The knowledge on the fracture behavior, cracking behavior and microstructural changes occurring at the DMW interface upon long-term plant operation and aging is lacking.

Carbides formed in the heat-affected zone (HAZ) of LAS can serve as fracture initiators, significantly impacting brittle fracture behavior [11,12]. Furthermore, phosphorus segregation to grain boundaries (GBs) and precipitates (e.g. carbides) can increase cracking susceptibility, promote GB decohesion and intergranular fracture, and elevate the ductile-to-brittle transition temperature (DBTT) [13–15]. Consequently, the P content in modern reactor LASs has been limited to 0.008 wt%. Recently, Lindqvist et al. [16,17] reported that in a modern SA508/Alloy 52 DMW, crack initiation and propagation in thermally-aged T_0 fracture toughness specimens occurred in the HAZ without the crack deviating to the FB, resulting in a significantly lower fracture toughness than for the specimens where the notch crack was placed near the FB and the crack path deviated to the FB. Understanding the elemental segregation and carbide evolution occurring in the HAZ of modern reactor LASs upon long-term thermal aging is critical for evaluating structural integrity and ensuring the long-term operation of nuclear components [18–21]. However, such information is scarce in the open literature [22–24].

In this paper, a full-scale DMW safe-end mock-up, precisely replicating a critical component of a modern nuclear power plant, was studied. The brittle fracture behavior, carbide evolution and nanoscale elemental segregation in the LAS HAZ were analyzed under post-weld heat-treated and thermally-aged conditions (equivalent to 90 years of operation) using analytical electron microscopy and atom probe tomography (APT). The intrinsic interaction of nanoscale elemental segregation and carbide coarsening with the GB decohesion and the decrease of fracture toughness was discussed.

* Corresponding author.
E-mail addresses: pedro.ferreiros@vtt.fi (P.A. Ferreirós), yanling.ge@vtt.fi (Y. Ge), song.lu@vtt.fi (S. Lu), mattias.thuvander@chalmers.se (M. Thuvander), zaiqing.que@vtt.fi (Z. Que).

https://doi.org/10.1016/j.matchar.2024.114419
Received 29 July 2024; Received in revised form 4 September 2024; Accepted 28 September 2024
Available online 30 September 2024

2. Materials and method

In the present study, a 1:1 scale narrow-gap gas tungsten arc welding (GTAW) DMW mock-up, joining an SA508 Gr.2 nozzle with a 316LN safe-end using Alloy 52 filler metal, representative of a critical component in a modern Nordic nuclear power plant [25–27], is studied. The chemical composition of the materials is provided in Table 1. The mock-up is welded one bead per layer by gas tungsten arc welding (GTAW). The mock-up was post-weld heat treated at 550 °C for 15 h and 610 °C for 7 h. The studied conditions include the as-received post-weld heat-treated condition ("AR") and the long-term thermally-aged condition of 15,000 h at 400 °C ("TA"), purposely equivalent to 90 years of operation at 288 °C in a nuclear power plant [15].

For characterization of the fracture toughness T_0 reference temperature for the DBTT region according to ASTM E1921, 5 × 10 × 50 mm single edge-notched side-grooved bend (SE(B)) specimens were tested. The cracks of the SE(B) specimens are nominally located in the HAZ of the LAS, 0–350 μm from the FB. The cracks are parallel to the FB. Before testing, the specimens were pre-cracked by fatigue to the initial crack length over a specimen width ratio a_0/W of 0.5, using a RUMUL resonant testing machine. The maximum value of the applied stress intensity factor, K_{max}, was kept below 15 MPa$\sqrt{m}$ during the fatigue pre-cracking. The fracture toughness testing was performed using an MTS universal servo-hydraulic testing machine equipped with a 10 kN load cell. The crack mouth opening displacement (CMOD) was measured using an Epsilon 3541-003 M-040 M-LHT clip gauge. After testing, the specimens were soaked in liquid nitrogen and broken into two halves to measure the crack lengths. The crack length and crack front straightness were checked before calculation of T_0. The quality of the results was assessed after testing. All the T_0 specimens fractured by the brittle fracture mechanism and the brittle fracture initiated without significant ductile crack growth.

The prior austenite grain (PAG) size was evaluated with electron backscatter diffraction (EBSD). A Zeiss Crossbeam 540 scanning electron microscope (SEM) with an EDAX HikariPlus EBSD detector was applied. EBSD was performed with a working distance of 14–15 mm, a step size of 150 nm and with the samples tilted at 70°. The resulting EBSD inverse pole figure (IPF) was analyzed with the TSL OIM Analysis 8.6 software. The Vickers micro-hardness measurements with loads of 0.1 kg (HV0.1) across the FB were performed using a Struers DuraScan-80 device.

To assess the microstructure and the carbides in the LAS HAZ, lamellae were prepared using focused ion beam (FIB) with JEOL JIB 4700. The lamellae were investigated using a Thermo Fisher Talos F200X analytical transmission electron microscope (TEM), equipped with the Super-X Energy-dispersive X-ray spectroscopy (EDS) system, operating at 200 kV. High-angle annular dark-field (HAADF) and bright field (BF) images were recorded.

For nanoscale chemical analysis of GBs, APT was performed. EBSD maps collected on a TESCAN GAIA3 equipped with an Oxford-NordlysNano detector were used to investigate the GB misorientations on AR and TA samples. This allowed to identify sites of interest for the APT lift-outs – high-angle GBs with comparable misorientation angles (55–60°). Site specific APT sample preparation was conducted on a dual-beam FIB-SEM FEI Versa 3D workstation. The back-scattered electron signal was used to find the previously identified sites of interests, and to guide during the tip sharpening step allowing to place the targeted GB in the proximity of the needle apex. Transmission Kikuchi Diffraction (TKD) was performed on the sharpened specimens to confirm the presence of the GBs and to verify their misorientation angles before APT measurement. TKD was performed on a TESCAN GAIA3, in STEM mode, equipped with Oxford-NordlysNano detector. All APT measurements were conducted on a CAMECA LEAP 6000 XR in laser mode, at 50 K specimen temperature, 50–70 pJ laser energy, 0.3 % evaporation rate. Auto pulse frequency control was set to collect a minimum mass-to-charge ratio of 150 Da. The CAMECA APT Suit 6 software was employed to create reconstructions and evaluate the data.

3. Result and discussion

The EBSD maps revealing the grain structure in the HAZ as a function of the distance to the FB in the AR and TA samples are shown in Fig. 1. The macrostructure of the DMW mock-up studied is presented in Fig. 2 (a). The HAZ adjacent to the FB is estimated to be about 2.5 mm wide. Fig. 2(b) illustrates the variation in micro-hardness and PAG size as a function of distance from the FB in the LAS HAZ under both AR and TA conditions. The hardness reaches a maximum and the grain size a minimum at 0.3–0.5 mm from the FB, i.e. in the grain-refined region. For the T_0 fracture toughness TA specimens, with crack propagation occurring in the HAZ (~0.3–0.5 mm from the FB) without deviation to the FB, a significantly lower (~1/3) fracture toughness was observed in comparison to specimens where the notches were placed near the FB and with the cracking path deviating to the FB. A summary of the T_0 testing results and representative cross-sectional characterizations is shown in Fig. 2(c-e). While the FB in the DMW is typically considered the most vulnerable location regarding fracture mechanical behavior, this study revealed a much lower local brittle fracture toughness in the HAZ at a distance of approximately 0.3–0.5 mm from the FB.

Representative fracture surfaces of the T_0 fracture toughness specimens in the AR and TA materials are shown in Fig. 3. The AR material exhibits brittle fracture with cleavage facets, while the TA material shows intergranular cracking. This reveals that long-term thermal aging increases GB decohesion and intergranular cracking, resulting in a decreased fracture toughness in the LAS HAZ of the TA specimens.

The carbide distribution in the HAZ (at a distance of approximately 0.3 mm from the FB) of the AR and TA materials is illustrated in Fig. 4. In the HAZ, the volume fraction of carbide increases upon thermal aging. Analytical scanning transmission electron microscopy (STEM), EDS maps and extracted elemental line profiles (Fig. 4(a)) reveal two types of carbides in the LAS HAZ of the AR material. The dominant and larger carbides are (Fe, Mn, Cr)$_3$C carbides (θ-M$_3$C type), located both at GBs and within grains, with lengths ranging from tens to 150 nm and widths of 30–80 nm. Smaller carbides are Mo-rich (Mo$_2$C), located at GBs with a few tens of nm in size. In the HAZ of the TA material, the large carbides remain (Fe, Mn, Cr)$_3$C, with lengths extending up to 350 nm, as shown in the STEM-EDS maps in Fig. 4(b). Most Mo-rich carbides are still with sizes around a few tens of nm, though some exceed 100 nm. Thermal aging did not alter the types of carbides but resulted in their coarsening in the HAZ.

The effect of long-term thermal aging on the segregation of P and other alloying elements in the HAZ of LAS was investigated with APT. Given that the extent of segregation is closely linked to the misorientation angle of the GBs [28,29], this study focuses on comparing the elemental concentrations at high-angle GBs with similar misorientation (55–60°) located ~0.3 mm from the FB in both AR and TA conditions. Site specific APT needles were prepared with the FIB lift-out technique [30]. TKD was performed on the sharpened specimens to verify the GB misorientation angles before APT measurements, with the resulting representative maps shown in the Fig. 5.

Table 1
Chemical composition of the Alloy 52 weld and the DMW LAS nozzle (wt%).

	C	Al	Si	P	S	Ti	Cr	Mn	Fe	Ni	Cu	Mo
Alloy 52	0.023	0.66	0.15	<0.005	0.0007	0.54	29.9	0.26	10.4	Bal.	<0.01	<0.01
SA508	0.18	0.02	0.19	0.005	0.001	0.002	0.12	1.49	Bal.	0.78	0.06	0.49

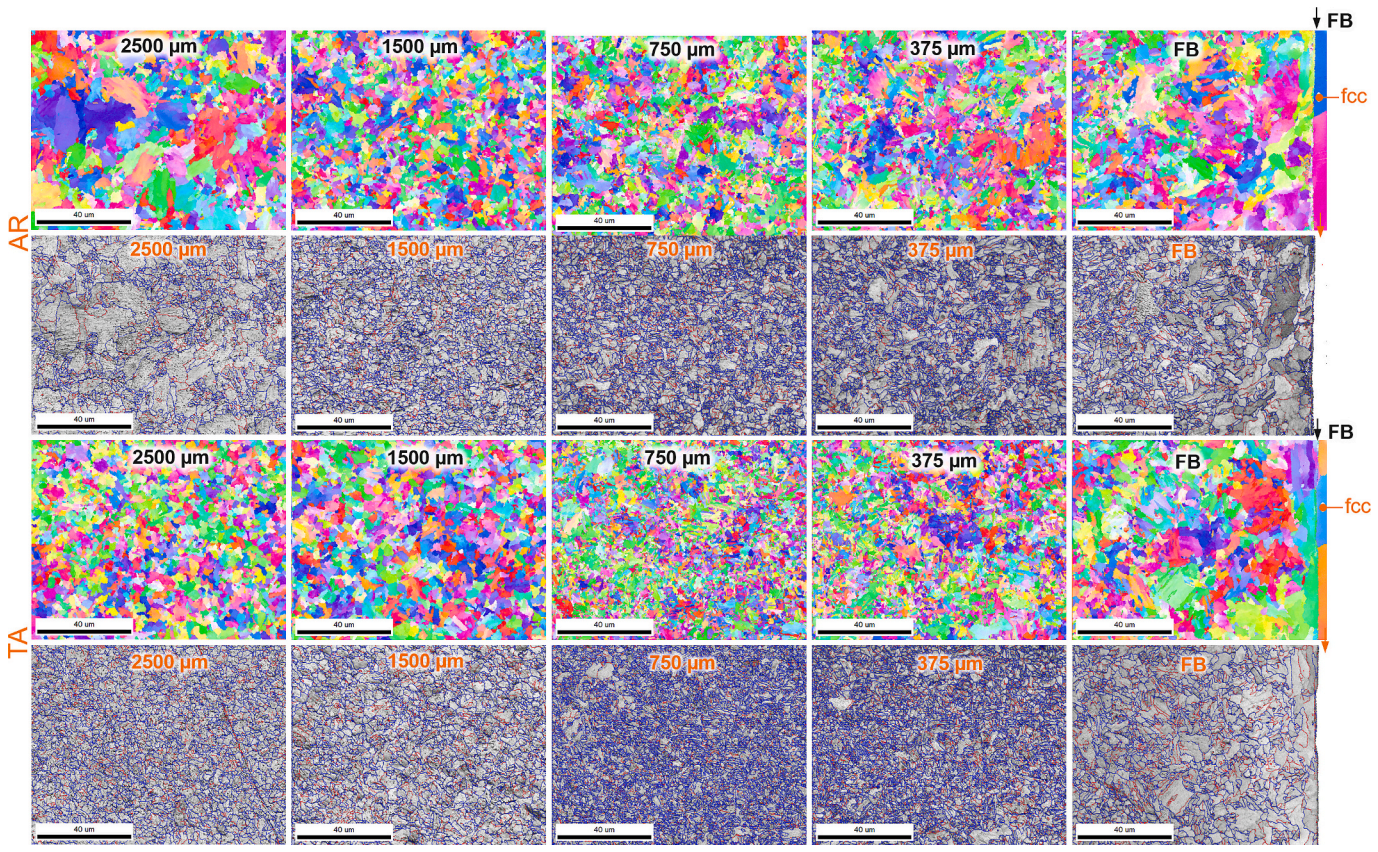

Fig. 1. EBSD IPF and image quality maps (rotation angle 2–15° in red and >15° in blue) per distance to the FB in the AR and TA samples. (For interpretation of the references to colour in this figure legend, the reader is referred to the web version of this article.)

Multiple APT measurements were conducted on both AR and the TA materials. Representative reconstructions of APT measurements from AR and TA materials are shown in Fig. 6(a-b). In the AR condition, there is only a very limited tendency for P to segregate at GBs, whereas significant P segregation is observed in the TA material. Other elements, such as Mo, C, and Mn, are found to segregate at GBs in both AR and TA materials. Fig. 7(a-b) display 1D concentration profiles across two GBs, showing the absence of P in the AR GB but up to 0.3 at.% P in the TA GB. Mo, Mn, and C are segregated in both AR and TA materials, but their concentrations at TA GBs are markedly higher.

Moreover, more and larger carbides can be found at GBs in the TA material in comparison to the AR material, as APT analysis of AR specimens showed no visible carbides associated with GBs, whereas significant carbides were observed in needles from TA specimens. Similar observations were made by the STEM analysis. A proximity histogram displaying the concentration of various elements at progressive distances from the surface of the Mo-carbide is presented in Fig. 7 (c). This plot indicates the composition inside the carbide, with approximately 60 at.% Mo and 30 at.% C, suggesting it is a Mo_2C-type carbide. Notably, Mo and C were found clustering along elongated features (likely dislocations or disconnections [31]) in the AR material, as visible in the right box in Fig. 6(a). This might highlight the tendency of these two elements to react and form carbides, potentially representing a nucleation stage for the Mo_2C carbides found in the TA material. Additionally, Cu-rich clusters, as observed by Medouni et al. [32] upon long-term aging, were not detected in this study. This discrepancy may be due to the lower Cu content in the current study (0.06 vs. 0.098 wt%).

Gibbsian interfacial excess (Γ) [33] for P, C, Mo, and Mn segregating at the GB of the AR and TA samples respectively has been calculated and reported in Table 2. As displayed by the 1D profiles and the Gibbsian interfacial excess, the segregation at the measured GBs is significant already in the AR sample. After TA, all elements accumulate further, particularly Mn and Mo. While C is expected to sit at interstitial sites, P, Mo and Mn are likely to be substitutional [34,35]. Mo plus Mn atoms reach a total value of Gibbsian interfacial excess around 16 atoms/nm^2. As comparison, the planar atomic densities of Fe-BCC (100) and Fe-FCC (111) are 12.17 atoms/nm^2 and 18.74 atoms/nm^2, respectively. Overall, after TA it is reasonable to imagine Mn and Mo forming a monoatomic layer at the GB. This can influence the mechanical behavior of the GB and affect the chemical environment potentially favoring the P segregation.

The results are consistent with our previous study [27], showing that the bulk P content in the HAZ grain interior is slightly higher in the AR material compared to the TA material, due to P segregation from the grain interior to GBs after thermal aging. The current APT analysis allows for calculating an approximate concentration of P in the grain interior, excluding contributions from GBs. These results, presented in Table 3, support the previously proposed hypothesis [27], with both studies reporting P concentrations in the same order of magnitude (tens of atomic ppm). In the current measurements, the bulk concentration of P in the AR material was around 20–50 ppm, aligning well with the previously measured range. However, the bulk concentration of P in the TA material measured in this work is lower than previously measured, possibly due to the region of interest selected for this study. The bulk composition presented in Table 3 was obtained by measuring P in regions around the selected HAGBs. The proximity to the GB and the P enrichment after thermal aging could be associated with a P depletion zone in the surrounding area, explaining the low *P* values measured in the supposed "bulk of the grain". Interestingly, the nominal P concentration for this alloy is around 90 atomic ppm, but both APT studies measured significantly lower bulk amounts of P even before aging. This might indicate some P segregation occurring before thermal aging, potentially at the interface with M_3C–type carbides, as suggested in our

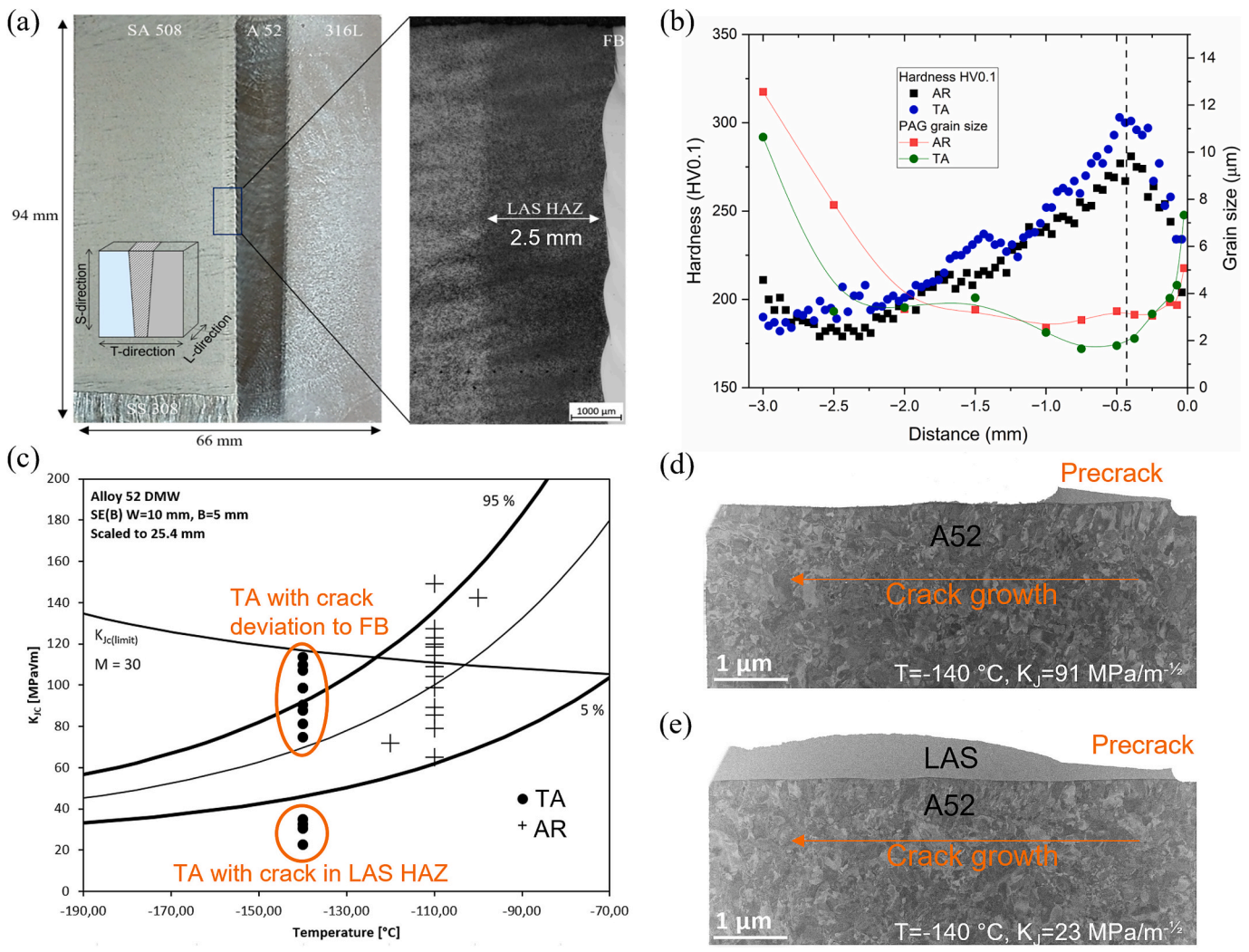

Fig. 2. (a) The investigated narrow-gap GTAW DMW mock-up. (b) The change in micro-hardness and PAG grain size in the HAZ of LAS adjacent to the FB. (c) Summary of the T_0 testing results for AR and TA materials. The representative cross-sectional characterizations of TA T_0 testing specimens (d) with and (e) without crack deviation to the FB. The deviation to the FB resulted in a much higher fracture toughness.

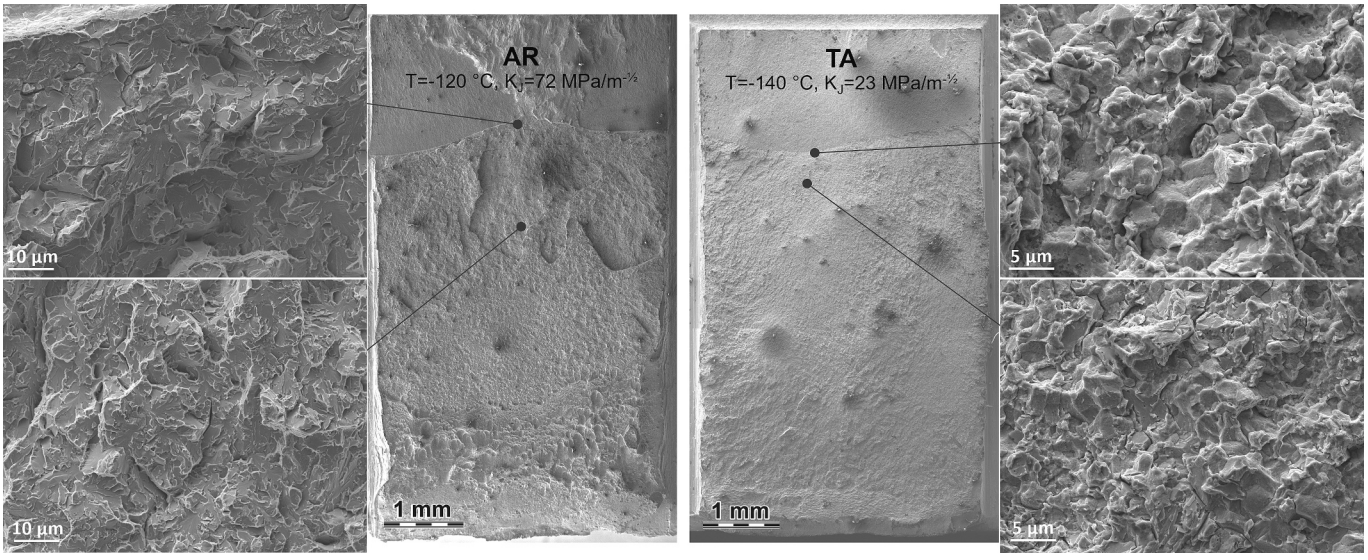

Fig. 3. Representative fracture surfaces of the T_0 fracture toughness specimens in the AR and TA materials.

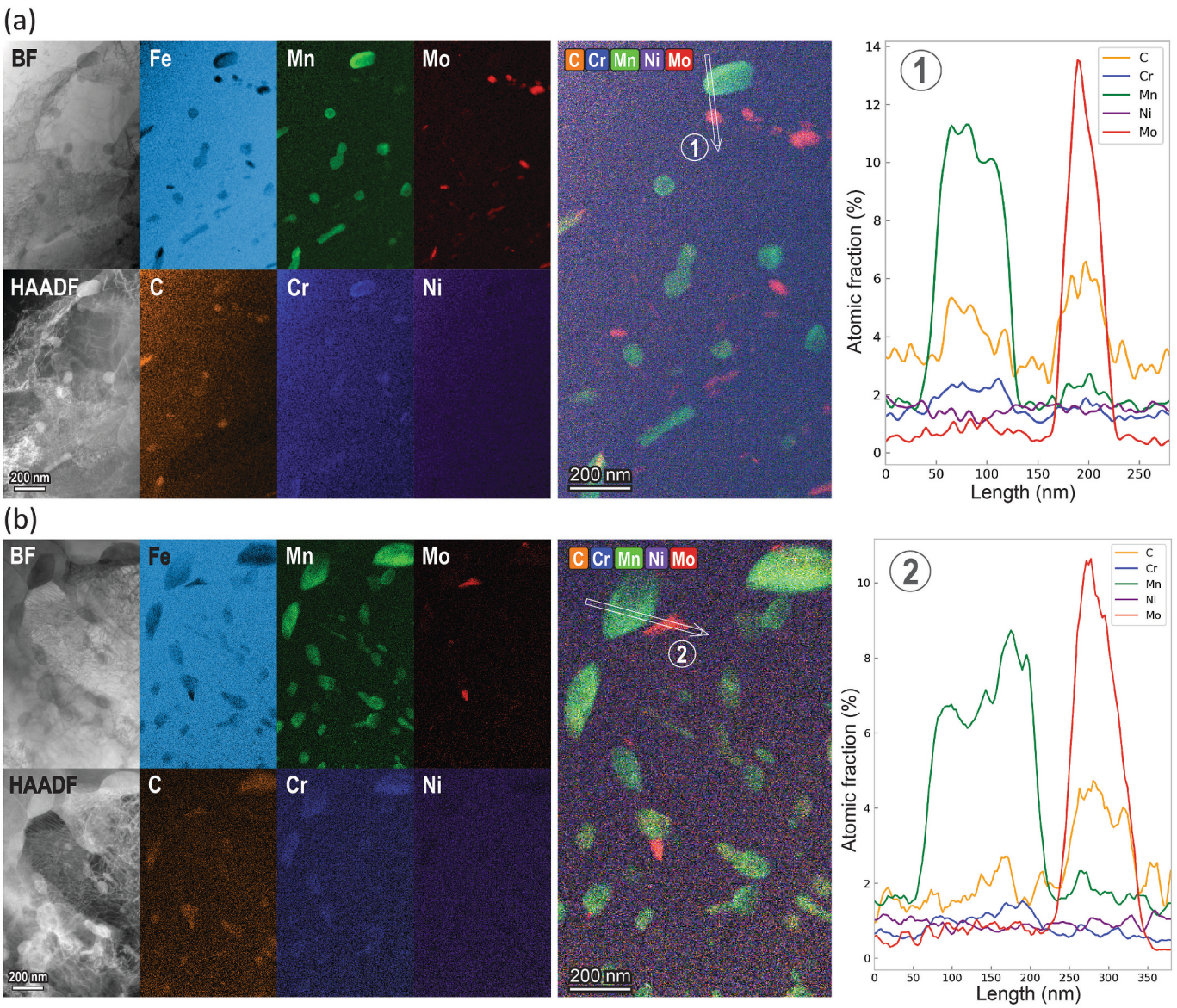

Fig. 4. Carbides in the LAS HAZ of (a) AR and (b) TA materials. The illustrative images are BF images, HAADF images, STEM-EDS elemental maps and extracted line profiles.

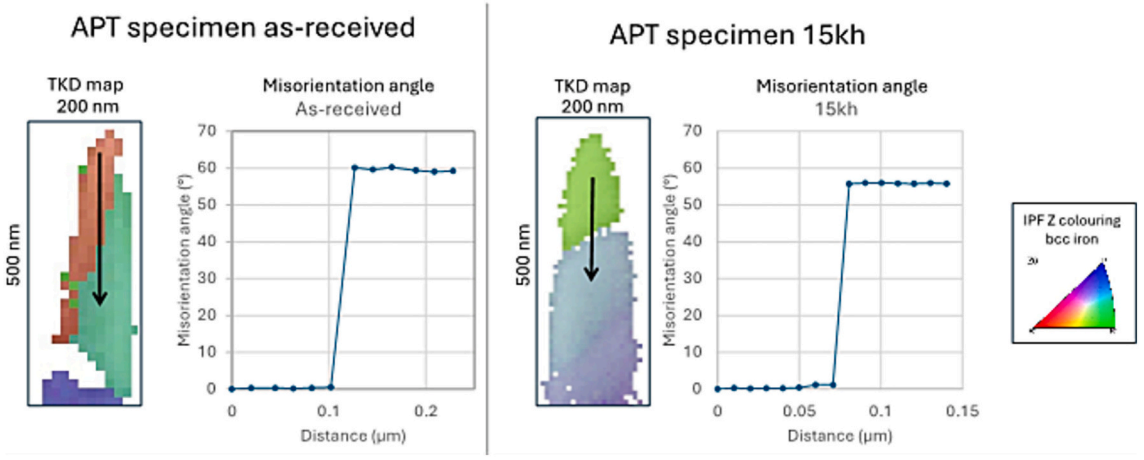

Fig. 5. Representative TKD maps of APT specimens: AR (left) and TA (right) material. High-angle GBs with comparable misorientation were selected.

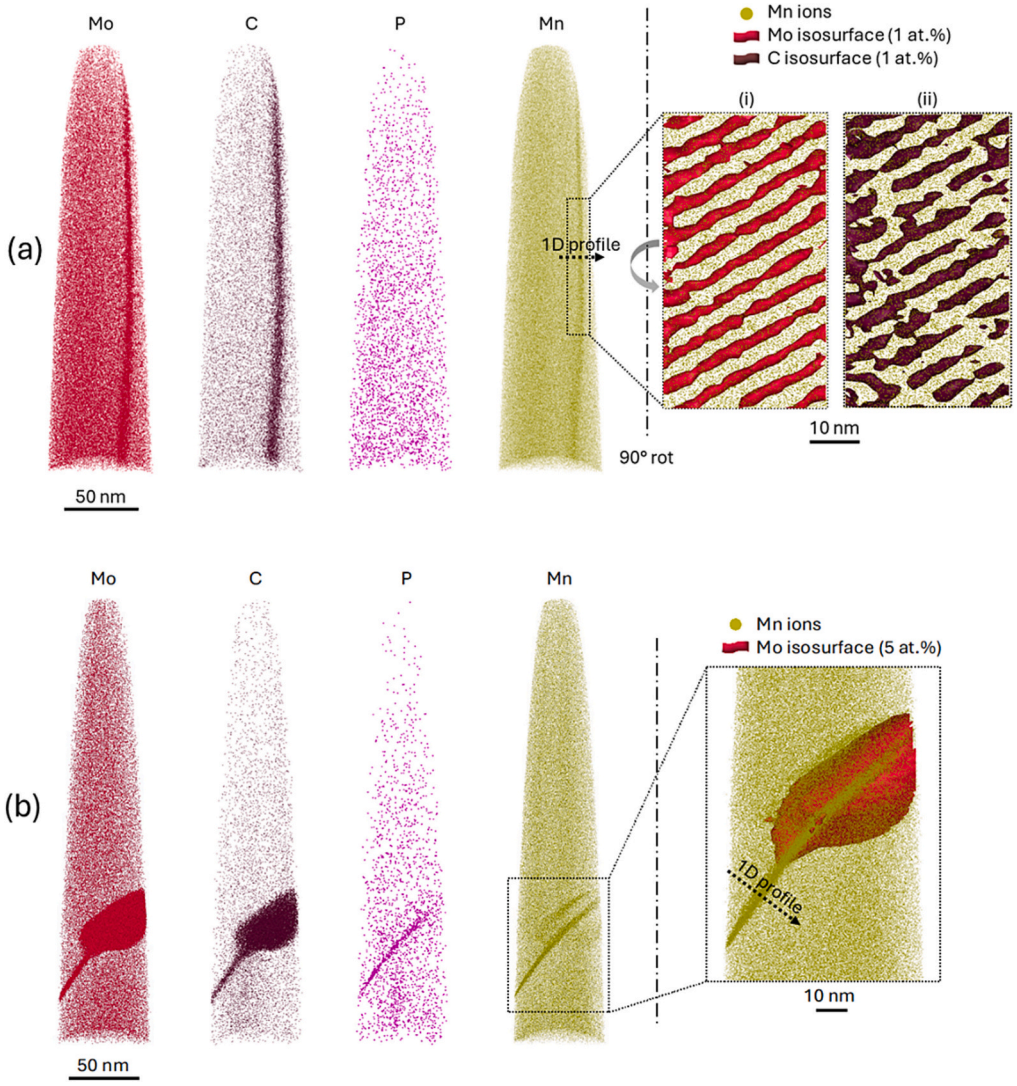

Fig. 6. 3D reconstruction of APT data collected across a HAGB in (a) AR material and (b) TA material. Atom maps of Mo, C, P and Mn are plotted. In (a), segregation of Mo, C and Mn (but no P) is evident from these maps. Segregation of Mo and C follows a pattern fitting enrichment at dislocations or disconnections arranged in a tight array as visible in the boxes to the right (Mo isosurfaces shown in (i), C isosurfaces shown in (ii)). In (b), segregation of Mo, C, P and Mn is evident from these maps. The presence of a Mo-carbide at the GB is evident, a detail of this feature is presented in the box to the right. The location and direction of 1D profiles (see Fig. 7) are indicated by the dashed arrows.

previous work [27].

The APT results on P and Mn segregation at GBs in AR and TA samples suggest that Mn segregation occurs earlier than P, likely due to the remarkably low P content in the material, consistent with previous observations by Kuzmina et al. [36]. In a Fe-9Mn ferritic steel with a P content less than 30 wppm, 10 min of tempering at 450 °C or 600 °C can already induce Mn segregation at GBs, but no P segregation was revealed by APT [36]. Mn segregation leads to a significant reduction in room-temperature impact toughness. The sole segregation of Mn itself in AR and TA samples should contribute to intergranular fracture, a known embrittlement effect of Mn in ferritic and duplex steels [36,37]. In LASs, Mn additions were observed to reduce the resistance to temper embrittlement [38], though the exact mechanisms are under debate. The proposed mechanisms are linked to the effect of Mn on the C activity, potential co-segregation of Mn and P, and the change of P diffusivity [38].

In terms of the interaction between Mn and P, Mn was found to increase P diffusivity and substantially modify the kinetics of P segregation in iron and steels [39,40]. Mn was also observed to enhance P segregation at GBs [41] and accelerate the temper embrittlement in LASs with the same P content [42]. The simultaneous increase in the segregation levels of P, C, Mn, and Mo in the TA sample, compared to the AR one, is consistent with previous experimental observations [43,44], which is often ascribed to the co-segregation mechanism [45] based on the presumed "attractive interaction" between P and other metal elements [43,46,47]. However, this contradicts ab initio results showing repulsive interactions between P and other transition metals (and with C as well) on a fundamental level [48–50]. As discussed by Suzuki et al. [51], a positive correlation between GB segregation of elements alone cannot prove co-segregation, which may also be attributed to the same GB structure dependence of elemental segregation. It appears that the segregation level at a GB is a competition between local GB structure, alloying element segregation energy, and solute interactions.

Ab initio calculations revealed a stronger P segregation tendency at general GBs (~ −1.0 eV) compared to other transition metals such as Mn, Ni and Mo (~ −0.5 eV) [48–50]. The repulsive interactions of P-Mn/Mo and P-C seem not strong enough to repel P atoms from segregation towards GBs, given the significant number of GB sites available and the low P content. Mai et al. [49] suggested that owing to the repulsive interactions and segregation binding, the enrichment of P

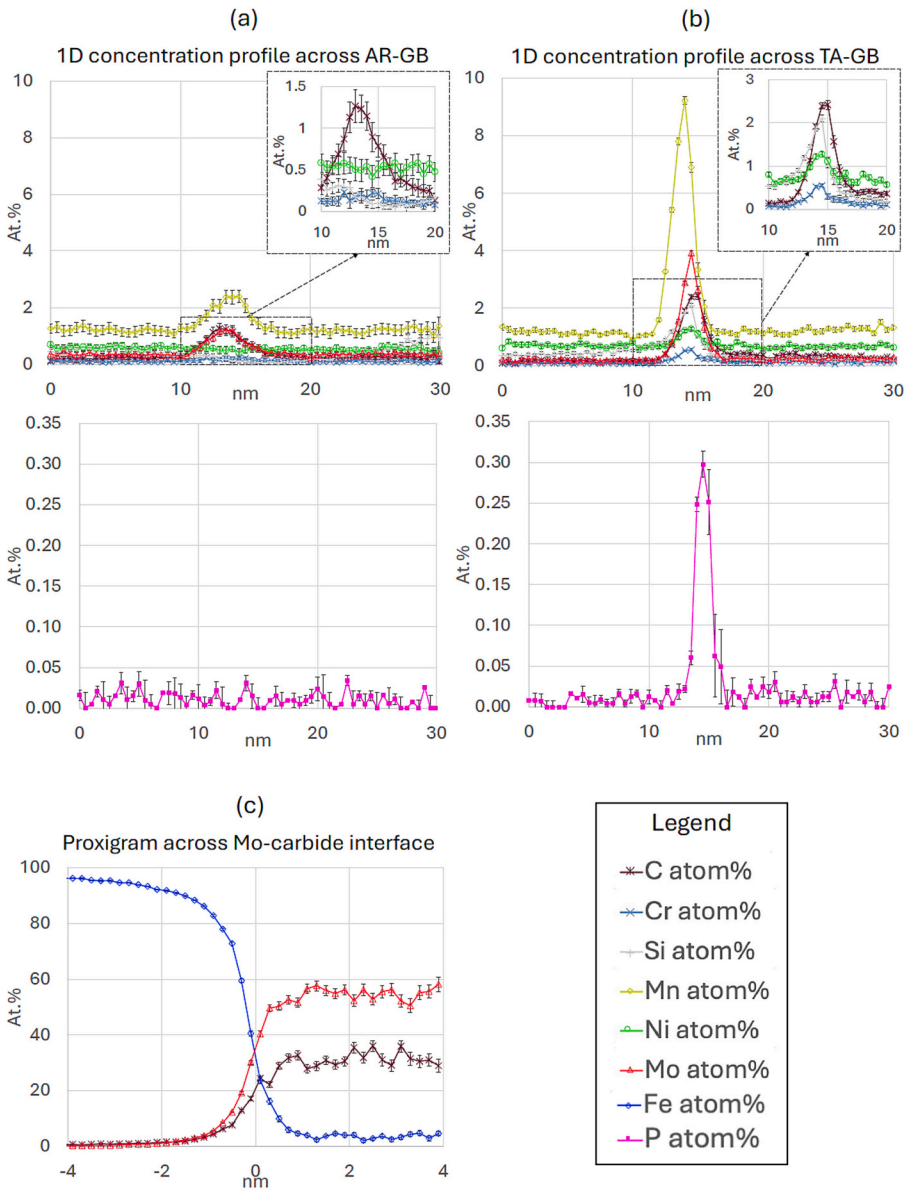

Fig. 7. 1D composition profile across HAGB in the AR material (a), main alloying elements are presented in the top plot while P is presented in the bottom plot. 1D composition profile across HAGB in the TA material (b), main alloying elements are presented in the top plot while P is presented in the bottom plot. Proximity histogram measured across the matrix–carbide interface for the carbide found in the TA material (c).

Table 2
Gibbsian interfacial excess (Γ) calculated for P, C, Mo, and Mn.

Specimen	Γ_P (atoms/nm^2)	Γ_C (atoms/nm^2)	Γ_{Mo} (atoms/nm^2)	Γ_{Mn} (atoms/nm^2)
AR	0.00	2.84	2.43	4.75
TA	0.29	3.01	4.16	12.46

Table 3
Bulk P content of AR and TA materials measured with APT (GBs were excluded).

	P (ppm)	P (wppm)
AR	32 ± 12	18 ± 7
TA	16 ± 4	9 ± 3

upon aging time results in a depletion of prior-segregated cohesion-enhancing solute elements at GBs, which critically influence the P-induced temper embrittlement. However, from the current experimental results, it appears that the segregation of Mn, Mo and C in the AR condition does not effectively repel P atoms from GB segregation upon extended tempering. On the other hand, when the segregation energy of one element is weak, such as Al in a ferritic steel, the strong repulsive interactions of C-Al and B-Al were sufficient to repel Al from GBs [52]. Strong C segregation is usually considered to suppress P-induced embrittlement, based on the C and P site competition mechanism, or the C-enhanced GB cohesion mechanism. Moreover, Mo is considered an element enhancing GB cohesion. In the present work, however, when C segregates to GBs and facilitates the formation and coarsening of carbides, it seems to weaken the resistance to temper embrittlement.

The reduction in brittle fracture resistance of DMWs can arise from inherent local inhomogeneities and increased constraint [22,53]. This

indicates that in the TA specimens, where the crack propagation occurred in the LAS HAZ at a distance of ~0.3–0.5 mm from the FB, the elemental segregation and carbide coarsening upon thermal aging contributed to the low resistance to brittle fracture. Long-term thermal aging at 400 °C for 15,000 h leads to coarsening of carbide precipitates and significant P and Mn segregation to GBs in the HAZ (despite a low bulk P content in modern low-P LASs). The carbide coarsening and segregation result in the presence of local brittle zones (additionally associated with peak nano-hardness and minimal grain size in HAZ), a higher degree of intergranular cracking and a low fracture toughness in the HAZ at a distance of ~0.3–0.5 mm from the FB. The direct observations of significant elemental segregation to GBs and the resultant reduction in fracture toughness in the HAZ are unexpected for modern low-P LASs. This should be considered for evaluating the long-term structural integrity of nuclear components.

4. Conclusions

The following conclusions can be drawn based on the obtained results:

- Long-term thermal aging results in significant P and Mn segregation to GBs (despite a very low bulk P content) and coarsens the carbides in the HAZ, which enhances GB decohesion, leads to local brittle zones, facilitates brittle crack propagation along GBs and ultimately causes a low fracture toughness.
- P can segregate to GBs in LAS after long service times even when its bulk content is very low. Simultaneously, Mn segregates at GBs and contributes to the intergranular fracture. It is observed that when C segregates to GBs and facilitates the formation and coarsening of GB carbides, it weakens the resistance to temper embrittlement.

CRediT authorship contribution statement

Andrea Fazi: Writing – review & editing, Writing – original draft, Methodology, Investigation, Formal analysis, Data curation. **Pedro A. Ferreirós:** Writing – review & editing, Methodology, Investigation, Formal analysis, Data curation. **Yanling Ge:** Writing – review & editing, Methodology, Investigation, Formal analysis, Data curation. **Song Lu:** Writing – review & editing, Investigation, Data curation. **Mattias Thuvander:** Writing – review & editing, Resources, Project administration, Methodology. **Zaiqing Que:** Writing – review & editing, Writing – original draft, Resources, Project administration, Methodology, Investigation, Funding acquisition, Formal analysis, Data curation, Conceptualization.

Declaration of competing interest

The authors declare that they have no known competing financial interests or personal relationships that could have appeared to influence the work reported in this paper.

Data availability

The data that support the findings of this study are available from the corresponding author upon reasonable request.

Acknowledgements

The authors wish to express their gratitude for the funding and support from Ringhals AB, OKG AB, Teollisuuden Voima Oyj and VTT Technical Research Centre of Finland within the FEMMA+ (Forum for the Effect of Thermal Aging and Microstructure on Mechanical and EAC Behavior of Ni-based Alloy Dissimilar Metal Welds+) research project. The authors also thank NKS for funding the NKS-FEMMA (AFT/NKS-R (24)134/2) project. The authors would like to thank P. Arffman, J. Lydman, J. Lukin and L. Sirkiä for the experimental contributions. The authors would further like to thank U. Ehrnstén, P. Efsing, B. Forssgren, H. Reinvall and H. Hänninen for suggestions and discussions. The APT experiments were performed at Chalmers Materials Analysis Laboratory (CMAL).

References

[1] M. Ahonen, S. Lindqvist, T. Sarikka, R. Mouginot, E. Leskelä, J. Lydman, U. Ehrnstén, P. Nevasmaa, T. Seppänen, P. Arffman, H. Hänninen, Thermal ageing and mechanical performance of narrow-gap dissimilar metal welds, VTT Technol. 333 (2018).
[2] W.-C. Chung, J.-Y. Huang, L.-W. Tsay, C. Chen, Microstructure and stress corrosion cracking behaviour of the weld metal in alloy 52-A508 dissimilar welds, Mater. Trans. 52 (1) (2011) 12–19.
[3] A. Akhatova, F. Robaut, M. Verdier, M. Yescas, F. Roch, C. Tassin, H. Landeghem, Microstructural and mechanical investigation of the near fusion boundary region in thermally aged 18MND5 / alloy 52 narrow-gap dissimilar metal weld, Mater. Sci. Eng. A 788 (139592) (2020).
[4] Z. Chen, Y. Lu, TEM observation of Martensite layer at the weld Interface of an A508III to Inconel 82 dissimilar metal weld joint, Metall. Mater. Trans. A 46A (2015) 5494–5498.
[5] M. Ahonen, R. Mouginot, T. Sarikka, S. Lindqvist, Z. Que, U. Ehrnstén, I. Virkkunen, H. Hänninen, Effect of thermal ageing at 400°C on the microstructure of ferrite-austenite interface of nickel-base alloy narrow-gap dissimilar metal weld, Metals 10 (3) (2020) 421.
[6] J. Parker, G. Stratford, Characterisation of microstructures in nickel based transition joints, J. Mater. Sci. 35 (2000) 4099–4107.
[7] J. Hou, Q. Peng, Y. Takeda, J. Kuniya, T. Shoji, J. Wang, E.-H. Han, W. Ke, Microstructure and mechanical property of the fusion boundary region in an alloy 182-low alloy steel dissimilar weld joint, J. Mater. Sci. 45 (2010) 5332–5338.
[8] P. Efsing, B. Forssgren, R. Kilian, Root cause failure analysis of defected J-groove welds in steam generator drainage nozzles, in: Proceedings of the Twelfth International Conference on Environmental Degradation of Materials in Nuclear Power Systems-Water Reactors, 2005.
[9] A. Jenssen, K. Norrgard, J. Lagerstrom, G. Embring, C. Jansson, P. Efsing, Structural assessment of defected nozzle to safe-end welds in Ringhals-3 and -4, in: Proc. Fontevraud V Intl. Symp, 2000.
[10] P. Efsing, J. Lagerström, Analysis of a defected dissimilar metal weld in a PWR power plant, in: 10th Int Conf Nucl Eng, 2002.
[11] Z. Que, M. Lindroos, J. Lydman, N. Hytönen, S. Lindqvist, P. Efsing, P. Nevasmaa, P. Arffman, Brittle fracture initiation in decommissioned boiling water reactor pressure vessel head weld, J. Nucl. Mater. 569 (153925) (2022).
[12] K. Choi, S. Yoo, S. Kim, T. Kim, J. Ham, J. Lee, J. Kim, Microstructural evolution and corrosion behaviour of thermally aged dissimilar metal welds of low-alloy steel and nickel-based alloy, Corros. Sci. 153 (2019) 138–149.
[13] J. Gao, J. Tan, M. Jiao, X. Wu, L. Tang, Y. Huang, Role of welding residual strain and ductility dip cracking on corrosion fatigue behavior of alloy 52/52M dissimilar metal weld in borated and lithiated high-temperature water, J. Mater. Sci. Technol. 42 (2020) 163–174.
[14] J. Kim, K. Choi, C. Bahn, K. J.H, In situ Raman spectroscopic analysis of surface oxide films on Ni-base alloy/low alloy steel dissimilar metal weld interfaces in high-temperature water, J. Nucl. Mater. 449 (2014) 181–187.
[15] P. Joly, M. Yescas, E. Keim, Fracture toughness in the ductile-brittle transition and thermal ageing behavior of decarburized heat affected zone of Alloy 52 dissimilar metal welds of nuclear components, in: Proceedings of the ASME-2014 Pressure Vessel and Piping Conference, Anaheim, California, USA, 2014.
[16] S. Lindqvist, Z. Que, P. Nevasmaa, N. Hytönen, The effect of thermal aging on fracture properties of a narrow-gap alloy 52 dissimilar metal weld, Eng. Fract. Mech. 281 (109056) (2023).
[17] S. Lindqvist, N. Hytönen, L. Sirkiä, P. Arffman, J. Lydman, Y. Ge, P. Nevasmaa, Z. Que, Fracture in the Ductile-To-Brittle Transition Region of A Narrow-Gap Alloy 52 and Alloy 52 Dissimilar Metal Weld With Buttering, in: ASME PVP2022–80690, Las Vegas, USA, 2022.
[18] R. Mouginot, Effect of Thermal Ageing on Alloys 690 and 52 in Pressurized Water Reactor Applications, Doctoral dissertation, Aalto University, 2017.
[19] H. Wang, G. Wang, F. Xuan, S. Tu, Fracture mechanism of a dissimilar metal welded joint in nuclear power plant, Eng. Fail. Anal. 28 (2013) 134–148.
[20] Z. Que, S. Lindqvist, N. Hytönen, Y. Ge, P. Nevasmaa, J. Lydman, L. Sirkiä, P. Arffman, A. Forsström Ja, U. Ehrnstén, Forum for the Effect of Thermal Aging and Microstructure on Mechanical and EAC Behaviour of Ni-Base Alloy Dissimilar Metal Welds (FEMMA), VTT Technology, Espoo, Finland, 2023.
[21] N. Hytönen, Z. Que, S. Lindqvist, J. Lydman, Y. Ge, I. Virkkunen, U. Ehrnstén, P. Rautala, P. Efsing, B. Forssgren, Fusion Boundary Microstructure and Fracture Behaviour of a narrow-gap Alloy 52 Dissimilar Metal Weld and an Alloy 52 Dissimilar Metal Weld and an Alloy 52 Dissimilar Metal Weld with Buttering, in: International Symposium Contribution of Materials Investigations and Operating Experience to LWRs' Safety, Performance and Reliability, FONTEVRAUD 10, Avignon, France, 2022.
[22] H. Wang, G. Wang, F. Xuan, C. Liu, S. Tu, Local mechanical properties of a dissimilar metal welded joint in nuclear power systems, Mater. Sci. Eng. A 568 (2013) 108–117.

[23] S. Yoo, K. Choi, C. Bahn, S. Ki, J. Kim, J. Kim, Effects of thermal aging on the microstructure of type-II boundaries in dissimilar metal weld joints, J. Nucl. Mater. 459 (2015) 5–12.
[24] A. Blouin, S. Chapuliot, S. Marie, C. Niclaeys, J. Bergheau, Brittle fracture analysis of dissimilar metal welds, Eng. Fract. Mech. 131 (2014) 58–73.
[25] N. Hytönen, Y. Ge, Z. Que, S. Lindqvist, J. Lydman, U. Ehrnstén, P. Rautala, I. Virkkunen, P. Efsing, Effect of microstructure on mechanical behavior of Ni-base Alloy Dissimilar Metal Welds, in: The 20th International Conference on Environmental Degradation of Materials in Nuclear Power Systems-Water Reactor meeting, Colorado, USA, 2022.
[26] N. Hytönen, Y. Ge, Z. Que, S. Lindqvist, P. Nevasmaa, I. Virkkunen, P. Efsing, Study of fusion boundary microstructure and local mismatch of SA508/alloy 52 dissimilar metal weld, J. Nucl. Mater. 583 (154558) (2023).
[27] Y. Ge, Z. Que, K. Lindgren, N. Hytönen, M. Thuvander, Effect of thermal aging on microstructure and carbides of SA508/alloy 52 dissimilar metal weld, Mater. Charact. 200 (112880) (2023).
[28] L. Zhang, B. Radiguet, P. Todeschini, C. Domain, Y. Shen, P. Pareige, Investigation of solute segregation behavior using a correlative EBSD/TKD/APT methodology in a 16MND5 weld, J. Nucl. Mater. 523 (2019) 434–443.
[29] M. Thuvander, J. Weidow, J. Angseryd, L. Falk, F. Liu, M. Sonestedt, K. Stiller, H. Andren, Quantitative atom probe analysis of carbides, Ultramicroscopy 111 (6) (2011).
[30] K. Thompson, D. Lawrence, D.J. Larson, J.D. Olson, T.F. Kelly, B. Gorman, In situ site-specific specimen preparation for atom probe tomography, Ultramicroscopy 107 (2–3) (2007) 131–139.
[31] H. Khater, A. Serra, R. Pond, J. Hirth, The disconnection mechanism of coupled migration and shear at grain boundaries, Acta Mater. 60 (5) (2012) 2007–2020.
[32] I. Medouni, A. Portavoce, P. Maugis, M. Descoins, M. Yescas, F. Roch, P. Joly, K. Hoummada, Thermal ageing effect on solute segregation and precipitation in the heat-affected-zone of dissimilar metal welds for nuclear power plants, Mater. Des. 232 (112158) (2023).
[33] O. Hellman, D. Seidman, Measurement of the Gibbsian interfacial excess of solute at an interface of arbitrary geometry using three-dimensional atom probe microscopy, Mater. Sci. Eng. A 327 (1) (2002) 24–28.
[34] X. Song, K. Peng, Z. Yuan, J. Jia, J. Liu, L. Fan, Texture, grain boundary characterization and segregation of phosphorus in an annealed interstitial free steel, J. Iron Steel Res. Int. 21 (9) (2014) 844–848.
[35] I. Stark, G. Smith, H. Bhadeshia, The distribution of substitutional alloying elements during the bainite transformation, Metall. Trans. A. 21 (1990) 837–844.
[36] M. Kuzmina, D. Ponge, D. Raabe, Grain boundary segregation engineering and austenite reversion turn embrittlement into toughness: example of a 9 wt.% medium Mn steel, Acta Mater. 86 (2015) 182–192.
[37] S. Wessman, S. Hertzman, R. Pettersson, R. Lagneborg, M. Liljas, On the effect of nickel substitution in duplex stainless steel, Mater. Sci. Technol. 24 (3) (2008).
[38] S. Park, K. Lee, K. Min, M. Kim, B. Lee, Influence of the thermodynamic parameters on the temper embrittlement of SA508 Gr.4N Ni–Cr–Mo low alloy steel with variation of Ni, Cr and Mn contents, J. Nucl. Mater. 426 (1–3) (2012).
[39] J. Smith, J. Reynolds, H. Southworth, Influence of Mn on kinetics of P segregation in low-alloy steel, Metal Sci. 16 (9) (1982).
[40] T. Matsuyama, H. Hosokawa, H. Suto, Tracer diffusion of P in Iron and Iron alloys, Trans. Jpn. Inst. Metals 24 (8) (1983) 589–594.
[41] H. Grabke, Grain boundary segregation of impurities in iron and steels and effects on steel properties, in: Impurities in Engineering Materials, Routledge, New York, 1999.
[42] S. Park, M. Kim, B. Lee, D. Wee, Study on the segregation behavior in SA508 Gr. 4N low alloy steel, in: Transactions of the Korean Nuclear Society Spring Meeting, Jeju, Korea, 2009.
[43] Z. Zhai, Y. Miyahara, H. Abe, Y. Watanabe, Effects of thermal history and microstructure on segregation of phosphorus and alloying elements in the heat-affected zone of a low alloy steel, Metall. Mater. Trans. A 45 (2014) 6163–6172.
[44] J. Han, J. Seol, M. Jafari, J. Kim, S. Seo, C. Park, Competitive grain boundary segregation of phosphorus and carbon governs delamination crack in a ferritic steel, Mater. Charact. 145 (2018) 454–460.
[45] M. Guttmann, Equilibrium segregation in a ternary solution: a model for temper embrittlement, Surf. Sci. 53 (1) (1975) 213–227.
[46] M. Guttmann, P. Dumoulin, M. Wayman, The thermodynamics of interactive co-segregation of phosphorus and alloying elements in iron and temper-brittle steels, Metall. Trans. A. 13 (1982) 1693–1711.
[47] P. Dumoulin, M. Guttmann, M. Foucault, M. Palmier, M. Wayman, M. Biscondi, Role of molybdenum in phosphorus-induced temper embrittlement, Metal Sci. 14 (1) (1980) 1–15.
[48] J. Wang, M. Enomoto, C. Shang, First-principles study on the P-induced embrittlement and de-embrittling effect of B and C in ferritic steels, Acta Mater. 219 (117260) (2021).
[49] H. Mai, X. Cui, D. Scheiber, L. Romaner, S. Ringer, Phosphorus and transition metal co-segregation in ferritic iron grain boundaries and its effects on cohesion, Acta Mater. 250 (118850) (2023).
[50] S. Morita, First-principles calculations on co-segregation of p and transition metal elements at fe grain boundaries, Kobelco Technol. Rev. 40 (2023).
[51] S. Suzuki, M. Obata, K. Abiko, H. Kimura, Effect of carbon on the grain boundary segregation of phosphorus in α-iron, Scr. Metall. 17 (11) (1983) 1325–1328.
[52] A. Ahmadian, D. Scheiber, X. Zhou, B. Gault, C. Liebscher, L. Romaner, G. Dehm, Aluminum depletion induced by co-segregation of carbon and boron in a bcc-iron grain boundary, Nat. Commun. 6008 (2021).
[53] P. Nevasmaa, P. Holmström, P. Karjalainen-Roikonen, T. Sarikka, M. Ahonen, R. Mouginot, U. Ehrnstén, A. Brederholm, P. Aaltonen, H. Hänninen, Fracture mechanical characterisation of ferrite-austenite dissimilar metal welds (DMWs) for elevated temperature service in view of metallurgical mismatch, in: International Conference on Life Management and Maintenance for Power Plants, 2013. Helsinki.